Gas–water percolation of tight sandstone reservoirs with different pore types in the Ordos Basin

Jie He[1] · Bozun Liu[2] · Shiying Shao[2] · Lei Zhang[3] · Xuming Cheng[3] · Yong xia[4] · Yushuang Zhu[1]

Abstract

To investigate the percolation mechanism of tight sandstone reservoirs, qualitative and quantitative methods are applied to analyze the pore structure of the Ordos Basin through scanning electron microscopy and high-pressure mercury injection. Based on gas–water relative permeability data and the visualization of real sandstone models, a gas–water displacement experiment was carried out to simulate the percolation mechanism and fluid distribution of different pore types. The results show that: ① The percolation of different pore types varies greatly, and the irreducible water saturation decreases when the reservoir properties improve. The relative permeability of gas at an irreducible water saturation increases, the width of the two-phase percolation area increases, and the percolation ability is enhanced as the reservoir properties improve. ② The gas–water displacement mode changes from fingering to uniform displacement with the improvement of pore type, which is beneficial to the formation of effective reservoirs filled with natural gas under the same hydrocarbon generation conditions. ③ The time required for the pressure relief of samples with good reservoir properties is short, and the recovery is higher with the improvement of pore type. ④ The residual water in samples with a poor pore type increases, which decreases the relative permeability of gas and recovery. A reasonable development pattern should be carried out, and the production pressure difference should be strictly controlled to maximize productivity. This study provides theoretical guidance for the development of tight sandstone reservoirs in the Ordos Basin.

Keywords Tight sandstone reservoir · Pore type · Percolation · Sedimentary · Ordos Basin

List of symbols

K_{rg} ($S_w = S_g$)	Relative permeability of gas at isotonic point
K_{rg} (S_{wi})	Relative permeability of gas at irreducible water saturation
S_{gi}	Residual gas saturation
S_w ($S_w = S_g$)	Water saturation at isotonic point
S_{wi}	Irreducible water saturation

✉ Yushuang Zhu
  petroleum_gas@163.com

1   State Key Laboratory of Continental Dynamics/Department of Geology, Northwest University, Xi'an 710069, China

2   China National Oil and Gas Exploration and Development Corporation, Beijing 100034, China

3   Sulige South Operation Company of PetroChina Changqing Oilfield, Xi'an 710018, China

4   Taizhou Oil Production Plant of Sinopec East China Oil & Gas Company, Taizhou 225300, China

Introduction

The tight sandstone reservoir has strong heterogeneity, complex pore structure, and poor physical properties (porosity is generally less than 10%, permeability is less than 1mD), which makes it difficult to predict favorable exploration areas compared with conventional gas reservoirs (Al-Fatlawi et al. 2019; Dai et al. 2012; Dheyauldeen et al. 2021; Gao et al. 2021; Rafieepour et al. 2020; Zheng et al. 2023a). At the same time, the water saturation in these reservoirs is high affected by the pore throat structure, heterogeneity, and fracture, resulting in complex and diverse seepage trends (Liang et al. 2023; Wang et al. 2022; Zhang et al. 2018; Zhao et al. 2023; Zheng et al. 2019). In recent years, Shang et al. concluded that the stronger the heterogeneity, the worse the reservoir physical properties, the greater the difficulty of production (Shang et al. 2017). Li et al. quantitatively characterized that the relationship between unconventional reservoir heterogeneity and microfractures in the Sulige region using cluster analysis based on heterogeneous parameters (Li et al. 2012). Liu et al. concluded that the fine

pore throats and clay minerals increase the water film thickness and block the seepage channels, reducing the saturation of movable fluid (Liu et al. 2016). Previous studies mainly analyzed the relationship between pore throat characteristics and multiphase fluid flow with experimental parameters but failed to reveal the influence of pore throat characteristics on percolation qualitatively and quantitatively (Cai et al. 2016; Guo et al. 2023; He et al. 2023; Liu et al. 2020; Mohammadi et al. 2011; Shabani et al. 2014; Zheng et al. 2023b). Here, the He-8 reservoir in the southeastern Ordos Basin is taken as the research object. Based on the testing and analysis of gas–water seepage of a real sandstone model for microscopic visualization, qualitative and quantitative methods are combined to analyze the gas–water seepage of tight sandstone reservoirs from the microscopic point of view to provide a reference and theoretical basis for the effective evaluation of tight sandstone gas reservoirs and further improvement of recovery.

Geological setting

The Ordos Basin is a large cratonic basin with long-term stable development, including multiple rotations, located in the western part of North China (Liu and Xiong 2021). The formation dips are gentle, and there are few anticlines with good traps and large amplitudes (Dou et al. 2018b; Guo et al. 2018; Li et al. 2017). The tertiary tectonics mainly resulted in nose uplift, and the structure is relatively simple (Liu et al. 2017).

This research is located in He-8 section, which belongs to a typical tight sandstone reservoir, with delta front subfacies (Dou et al. 2018a, 2018b). According to the statistical results of sandstone thin sections, quartz sandstone and lithic quartz sandstone are developed in the study area (Fig. 1) (Guo et al. 2023; He et al. 2021b; Zou et al. 2012). The study area has

poor physical properties, strong heterogeneity, high water saturation, and large fluid seepage resistance. More information on the region is provided in attachment. So how to design development parameters to improve reservoir recovery has become an urgent problem to be resolved (Fig. 2).

Methods

The sandstone is dominated by a medium to coarse-grained structure, which is distributed between 0.3 mm and 1.2 mm of size. The roundness is mainly subangular, followed by subangular-subrounded and subrounded, no angular particles are seen, the interparticle contacts are mainly linear contacts, and a few are point–line contacts or concave–convex contacts. The type of cementation is mainly pore type,
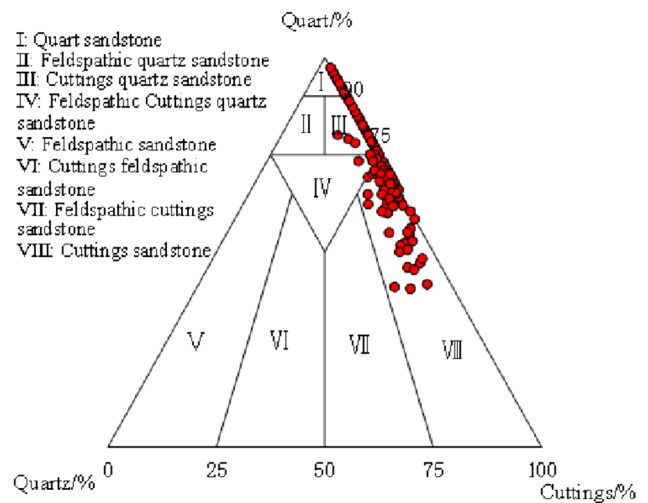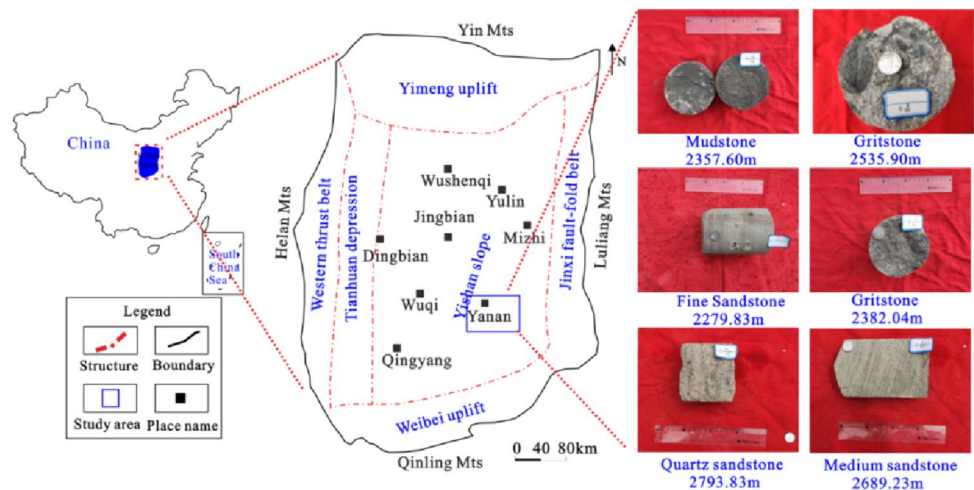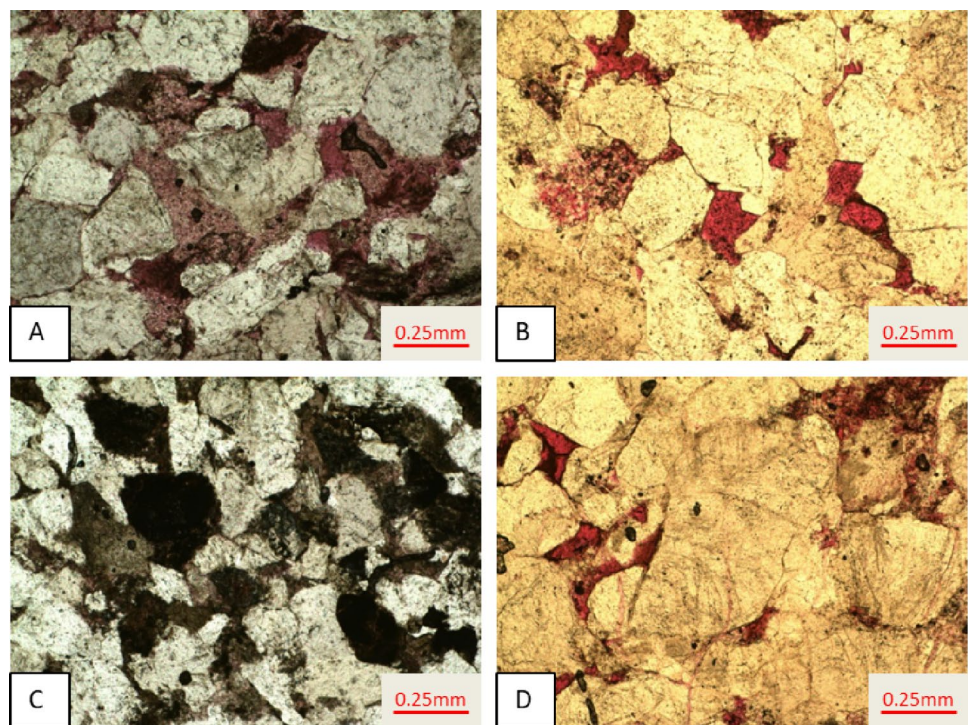

Fig. 2 Triangulation graph of types of sandstone reservoirs

Fig. 1 Location of the study area

Fig. 3 Photographs of thin sections

Table 1 Statistical table of the interstitial matter content of the reservoir

| Horizon	Interstitial matter/%						Total
	Illite	Kaolinite	Chlorite	Calcite	Silicious	Else	
Upper	3.63	2.28	0.82	1	3	0.1	10.83
Lower	4.97	2.62	0.3	1.1	4	0.2	13.19

followed by regeneration-pore type, and less film-pore type (Fig. 3).

The interstitial composition includes miscellaneous bases and cements (Dou et al. 2018a). The content of interstitial material in the layer of the study area ranges from 10.83 to 13.19% (Table 1) and is dominated by illite, kaolinite, and silica, with small amounts of chlorite and calcite. The illite content is the highest, accounting for 3.63% and 4.97%, respectively (Fig. 4).

Results

Micropore structure

The distribution, size, and connection of pore throats are the fundamental factors that determine seepage (Dou and Yang 2012; Zhou et al. 2022). Compared with those of conventional reservoirs, the pore shapes of the studied reservoir are more irregular and smaller.
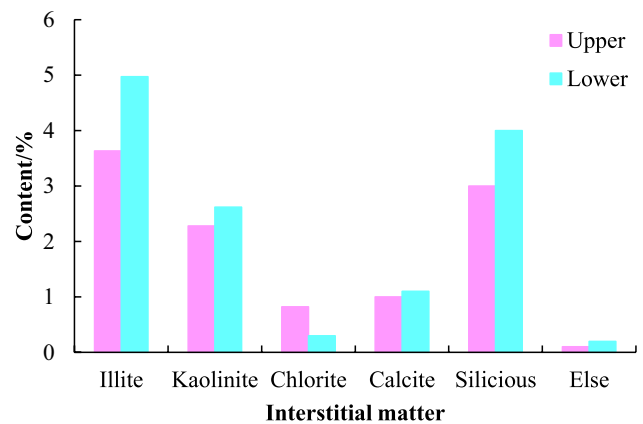
Fig. 4 Interstitial matter content of the reservoir

Pore throat type

The residual primary intergranular pores and intergranular dissolved pores are the most popular reservoir space, as shown in Table 2. The remaining pore types are less.

The results of the casting thin section analysis showed that the necked, dotted, and flaky types are mainly in the study area, with fewer curved flaky and bundled pore throats (Fig. 5).

Pore throat structure

Based on the experiment, it is concluded that there is a certain correspondence between the pore throat types observed from the mercury injection curve and the casting thin section (Wang et al. 2019). The pore throat structure characteristics are divided into four types (Table 3).

Table 2 Statistical table of reservoir space composition

Horizon	Primary pore/%	Secondary pores/%				
	Intergranular	Feldspar dissolution pore	Cuttings dissolution pore	Heterobasic dissolution pore	Intergranular pores	Microfractures
Upper	0.62	0.01	0.27	0.02	0.27	0
Lower	0.43	0	0.33	0.35	0.26	0.02
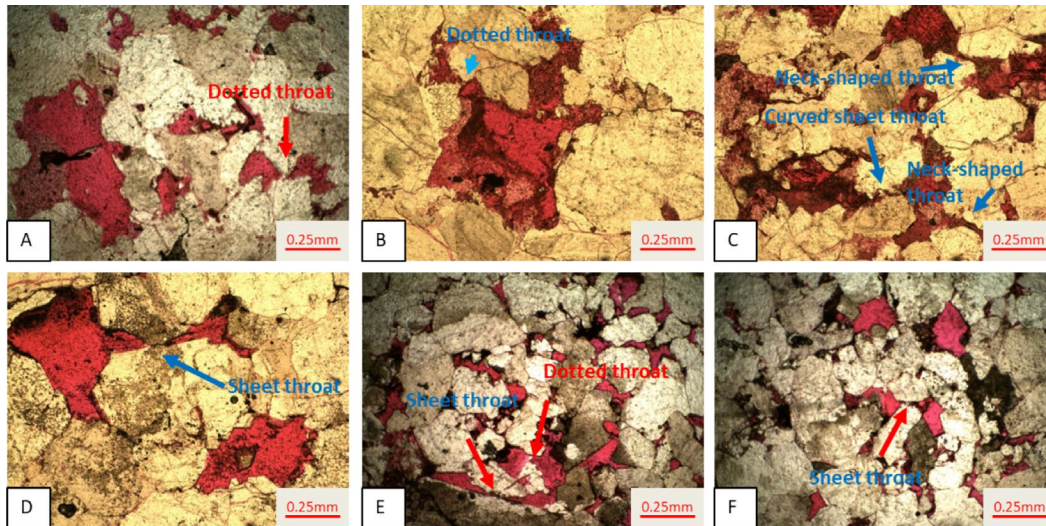
(A: Dotted pore throat; B: Dotted pore throat; C: Necked pore throat and curved flaky pore throat; D: Flaky pore throat; E: Flaky pore throat; F: Flaky pore throat)

Fig. 5 Types of pore throats (The red color is the experimental fluid, yellow is sandstone, and black color shows argillaceous sandstone). **A** Dotted pore throat; **B** Dotted pore throat; **C** Necked pore throat and curved flaky pore throat; **D** Flaky pore throat; **E** Flaky pore throat; **F** Flaky pore throat

Table 3 Parameters of the pore structure of the reservoir

Type		I	II	III	IV
Pore throat size	Displacement pressure/MPa	0.29–1.16/0.59	0.28–1.82/0.7	0.43–1.82/0.87	0.74–11.78/2.76
	Median pressure/MPa	1.92–11.8/4.41	2.17–13.98/5.98	1.27–35.92/12.21	11.57–139.5/71.14
	Average radius/μm	0.062–0.38/0.225	0.05–0.34/0.171	0.02–0.58/0.187	0.005–0.02/0.008
Pore throat sorting characteristics	Sorting coefficient	1.45–1.92/1.75	1.79–2.53/2.246	2.21–3.53/2.896	4.16–5.04/4.63
	Coefficient of variation	0.16–0.18/0.156	0.18–0.25/0.227	0.28–0.36/0.32	0.41–0.65/0.545
	Skewness factor	0.73–2.12/1.705	1.45–2.20/1.769	1.48–1.77/1.561	1.28–1.56/1.46
Pore throat connectivity	S_{Hg-max}/%	90.24–94.35/92.34	80.9–87.78/84.37	72.89–78.58/75.93	54.05–66.99/60.17
	Mercury removal efficiency/%	22.95–47.04/35.88	23.72–39.95/31.95	20.33–43.83/29.15	19.32–38/23.05

① Type I

The type I is intergranular pores with high mercury saturation, and the capillary pressure curve is concave and shifted to the left, high on the left and low on the right; the curve has an obvious platform. The average porosity is 6.6%, and the average permeability is 0.26×10^{-3} µm². The maximum mercury saturation ranges from 90.24 to 94.35%, with an average of 92.34%. The pore throat radius mainly ranges from 0.062 ~ 0.38 µm. The pore throats of this kind of pore structure are coarse, resulting in the best reservoir structure in terms of production potential (Fig. 6).

② Type II

The type II is intergranular dissolved pores. The mercury saturation is high, and the curve is slightly concave and shifted to the left, showing a gentle slope and a short platform. The average porosity is 3.5 ~ 8.97%, and the average permeability is $0.05 \sim 0.21 \times 10^{-3}$ µm². The displacement pressure is higher, mainly distributed from 0.28 ~ 1.82 MPa compared with type I. The pore throat distribution is coarse and skewed, indicating a better reservoir type in the study area (Fig. 7).

③ Type III

The type III is dissolved intercrystalline pores; the porosity ranges from 3% to 8.7%, and the permeability is $0.02 \sim 0.636 \times 10^{-3}$ µm². The displacement pressure is moderate. The capillary pressure curve is steeply sloped, the platform is not obvious, the pore throat radii are distributed from 0.02 to 0.58 µm, and the pore throat distribution has partial fine skewness and poor sorting. These findings suggest a poor reservoir in the study area (Fig. 8).

④ Type IV

The type IV is intercrystalline pores, with porosities of 0.79 ~ 4.53% and permeabilities of $0.001 \sim 0.167 \times 10^{-3}$ µm². The capillary pressure curve is lacking an obvious wide and gentle platform. The average displacement pressure is 2.76 MPa, the average pore throat radius is 0.008 µm, and the pore throat distribution is fine skewness with poor sorting (Fig. 9).

Percolation characteristics

Multiphase seepage

The curves can be classified into four categories according to the characteristics and parameters of the corresponding relative permeability curve (Table 4, Fig. 10) (Dou and Yang 2012; Su et al. 2014). Type I reservoirs have the
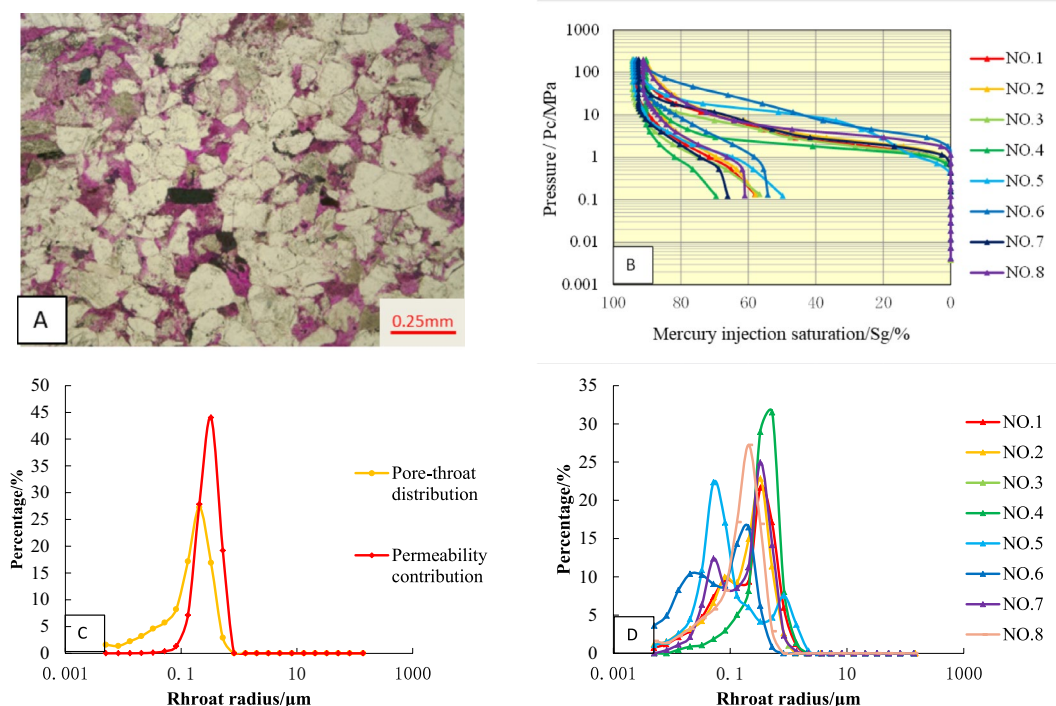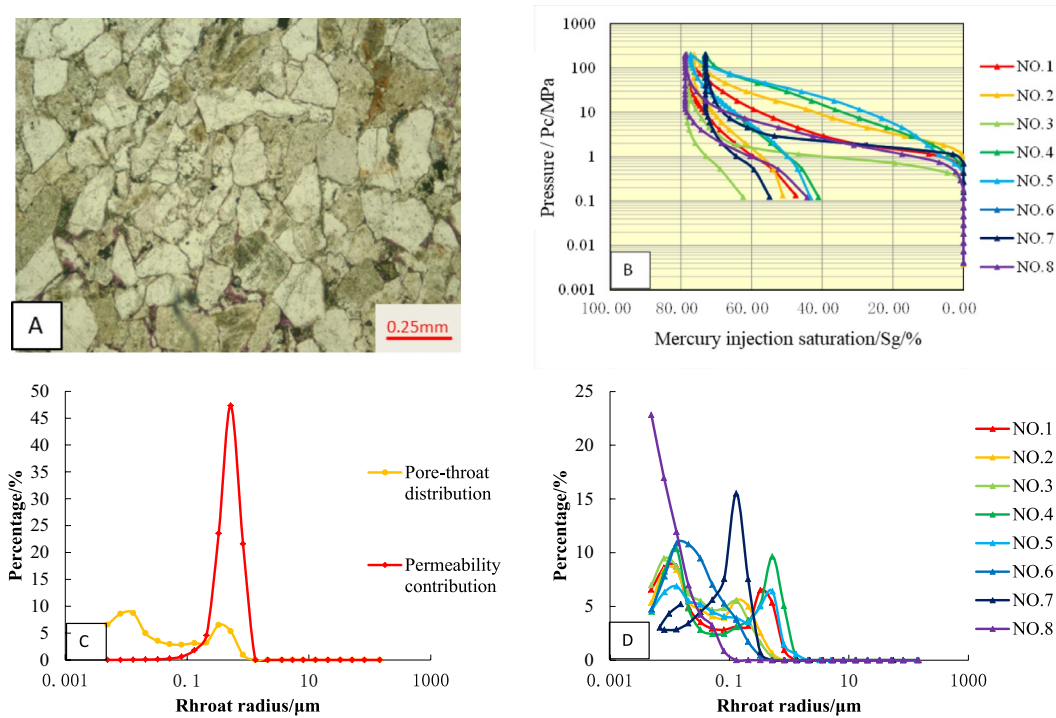

Fig. 6 Thin sections and pore throat distribution curves of type I reservoirs (**A** thin sections; **B** Mercury injection; **C** Pore throat distribution curve; **D** Pore throat distribution)
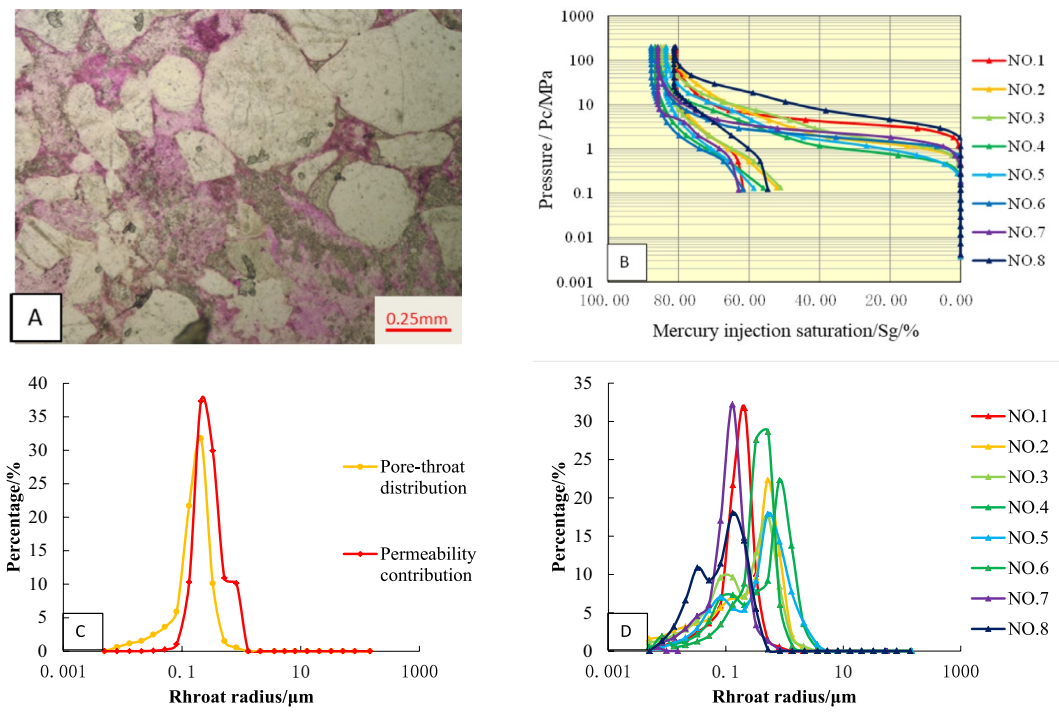
Fig. 7 Thin section and pore throat distribution curves of type II reservoirs (**A** thin section; **B** Mercury injection; **C** Shape of pore throat distribution curve; **D** Shape of pore throat distribution)
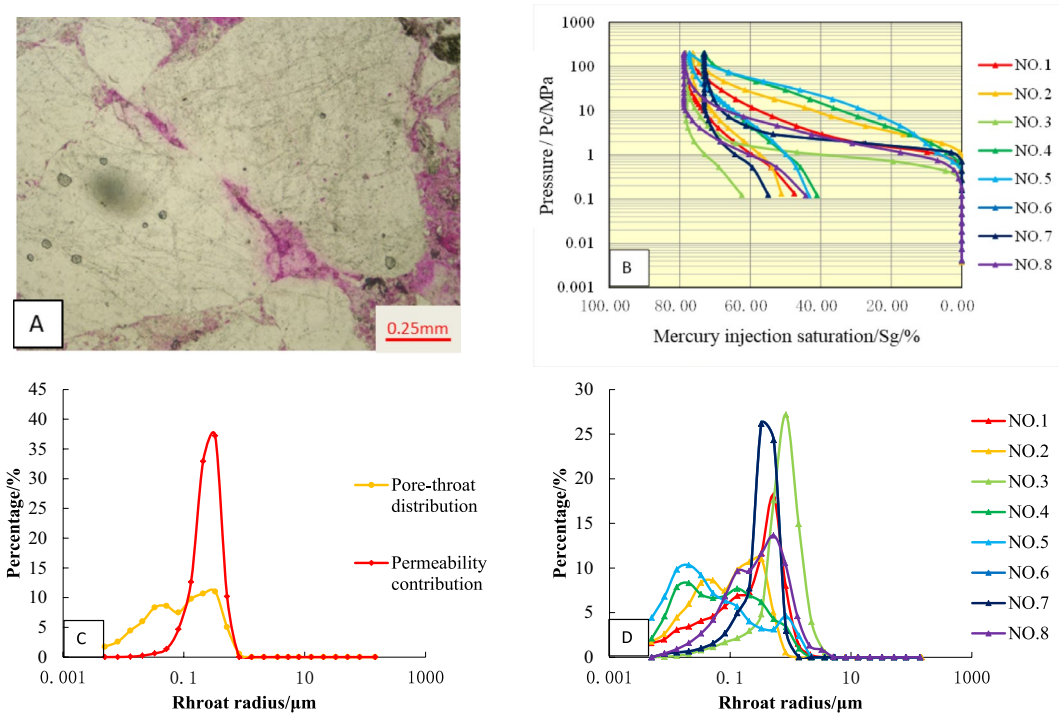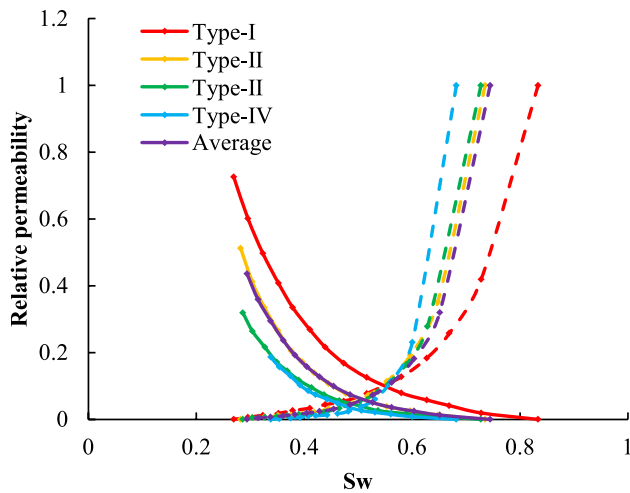

Fig. 8 Thin sections and pore throat distribution curves of type III reservoirs (**A** thin sections; **B** Mercury injection; **C** Pore throat distribution curve; **D** Pore throat distribution)

Fig. 9 Thin sections and pore throat distribution curves of type IV reservoirs (**A** thin sections; **B** Mercury injection; **C** Pore throat distribution curve; **D** Pore throat distribution)

Table 4 Characteristic parameters of the relative permeability

Type	Porosity/%	Permeability/10^{-3} μm^2	S_{wi}	K_{rg} (S_{wi})	S_w ($S_w = S_g$)	K_{rg} ($S_w = S_g$)	S_{gi}
Type I	10.98	0.30	0.274	0.487	0.495	0.079	0.246
	10.27	1.09	0.275	0.635	0.531	0.091	0.186
	9.64	8.94	0.269	0.726	0.548	0.103	0.167
	8.25	0.68	0.279	0.622	0.502	0.081	0.226
	7.99	0.54	0.282	0.637	0.505	0.081	0.238
Average	9.43	2.31	0.276	0.621	0.516	0.087	0.212
Type II	6.70	0.15	0.282	0.512	0.509	0.076	0.265
	5.84	0.10	0.319	0.394	0.500	0.041	0.295
	5.73	0.05	0.313	0.314	0.500	0.050	0.303
	5.07	0.11	0.287	0.424	0.500	0.053	0.273
Average	7.99	1.43	0.286	0.537	0.511	0.074	0.241
Type III	5.46	0.13	0.286	0.319	0.485	0.048	0.272
	5.37	0.05	0.317	0.313	0.502	0.060	0.312
	4.82	0.04	0.316	0.311	0.500	0.058	0.308
	4.58	0.03	0.337	0.191	0.495	0.032	0.322
Average	7.21	1.06	0.293	0.469	0.507	0.068	0.258
Type IV	4.52	0.02	0.316	0.320	0.493	0.049	0.309
	3.95	0.03	0.320	0.313	0.510	0.048	0.303
	3.55	0.01	0.338	0.186	0.493	0.032	0.318
Average	6.70	0.90	0.298	0.439	0.505	0.064	0.266

smallest irreducible water saturation, the widest range of the gas–water copermeability zone, and the highest isopermeability point. This type of reservoir has weak gas–water disturbance and strong fluid seepage ability (He et al. 2021a; Wu et al. 2021). From type II to III, the permeability of the gas–water isotonic point decreases gradually, and the

Fig. 10 Relative permeability curves

Fig. 11 Photographs of gas flooding in a real sandstone model of a reservoir (A1: type I; A2: type II; A3: type III; A4: type IV)

copermeability zone becomes narrower. The relative permeability curve of type IV has the lowest isotonic point in the lowest position, the smallest gas permeability at irreducible water saturation, the largest irreducible water saturation, and the smallest range of the two-phase copermeability zone. The reservoir's ability to store natural gas is proportional to the pore structure. Under the same hydrocarbon generation conditions, the pore structure is poor and complex, which is not conducive to the accumulation of natural gas and increases the resistance of fluid percolation.

Visual percolation

(1)   Characteristics of gas flooding

The results of gas–water visualization and percolation experiments show that the type I samples are dominated by uniform displacement, with a high displacement efficiency. Type II is dominated by uniform–reticular and reticular displacement. Type III is dominated by reticular–fingering displacement and fingering displacement. Tight reservoir type IV is mainly characterized by fingering displacement with low efficiency (Fig. 11).

Type I samples have high porosity and permeability and are dominated by uniform gas–water displacement. After pressurizing, the water is rapidly fingered forward and reaches the outlet; if the displacement pressure is reduced to below the outlet pressure, the water stops flowing, and the water still retains the original channel. At this time, if the pressure is increased again, the water still advances along the original channel, and the outlet pressure does not change.

The properties of the type II samples are moderate, and the displacement modes are uniform–reticular and reticular displacement. The gas enters the sample initially with
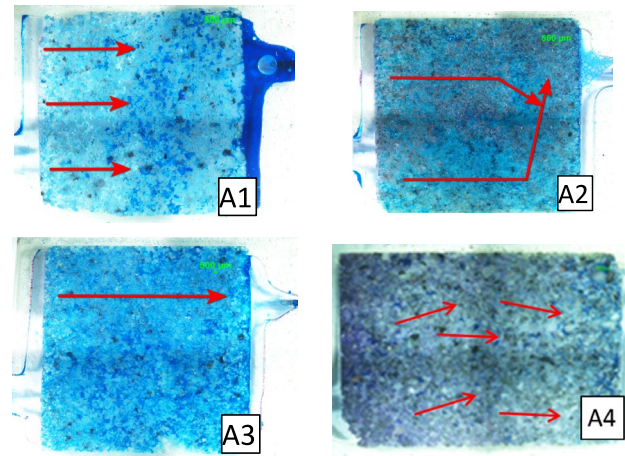
uniform percolation, and then the channels gradually change to form uniform–reticular or reticular displacement. Type II samples have necked pore throats and blind pores, and the gas will remain in the blind pores in the form of stuck bubbles. After pressurization, the water moves forward along the bottom and the range gradually expands.

Type III reservoirs have poor connectivity and high heterogeneity, and gas is displaced along high-permeability channels with low resistance. The seepage channel is not widened with increasing pressure, and more residual water is formed around the particles in the model.

Due to the compaction in tectonic movement and cementation in the diagenetic process, the type IV reservoir has poor properties, such as a low displacement speed and low displacement efficiency, mainly manifested as fingering displacement over a long pumping time, and the gas–water displacement effect is worse when there are water-sensitive minerals in the reservoir.

(2)   Characteristics of water flooding

At present, scholars in this field use the method to simulate the depletion production of gas reservoirs, which has the advantage of reflecting the interference between gas and water seepage but the disadvantage of being unable to describe water production and the influence of residual water on gas seepage (Clarkson et al. 2013; Dou and Yang 2012).

Since gas is colorless, it is difficult to observe the change in gas volume during the experiment, and it is necessary to judge the gas recovery based on the change in pressure. After the gas flooding state stabilized, the pressure at the outlet end of the model was first turned off, and the model was allowed to fill with pressure for a period to simulate the original pressure of the formation. Second, the inlet was

closed, and the outlet was opened to simulate the production of the well, during which the pressure drop time and drop volume were accurately recorded (Fig. 12).

Before the simulation, the occurrence mode of residual water mainly includes: ① cluster residual water, ② corner residual water, and ③ membrane residual water. Early in the simulation, the pressure drop rate is small, the drag force generated in the seepage has little effect on the residual water, and no seepage occurs from the membrane residual water and the corner residual water. In the middle and late stages of the simulation, the pressure continues to decrease, the momentum due to the expansion of the gas is greater than the percolation resistance, and part of the bound and membrane residual water becomes movable water.

Combined with the experimental results of the reservoir property analysis, it was concluded that the pressure relief time gradually increases from type I reservoirs to type IV reservoirs. As shown in Fig. 12, the reservoir properties are inversely proportional to the time of pressure relief and directly proportional to the degree of pressure drop. The reservoir properties are proportional to the degree of gas recovery and inversely proportional to the amount of residual gas during production, so wells with poor properties produce a small amount of gas or even no gas in the late period.

Discussion

The threshold pressure of the mercury injection curve reflects that the nonwetting phase (natural gas) can flow only by overcoming the influence of the starting pressure gradient. The threshold pressures of the type I, II, III, and IV pore structures obtained by high-pressure mercury injection experiments are 0.708, 0.922, 1.164, and 2.929 MPa, respectively. The capillary pressure under reservoir conditions is
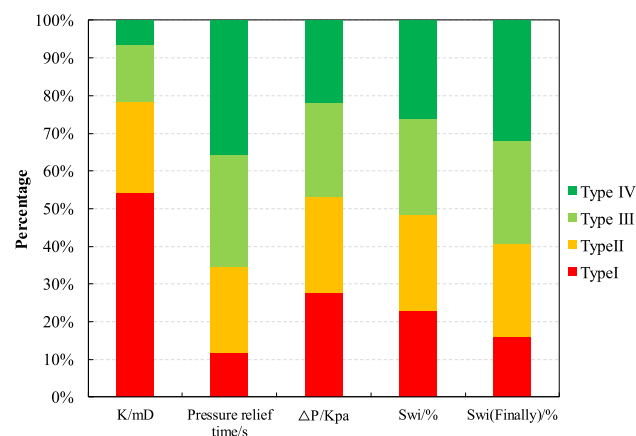
Fig. 12 Pressure−time curves of reservoirs with different pore types (K: Permeability; ΔP: Pressure difference)

approximately half that under the test conditions; that is, the natural gas (nonwetting phase) in the reservoir can be recovered when the pressure difference of the four pore types is at least 0.35, 0.46, 0.58, and 1.46 MPa.

The original water saturation of the reservoir is affected by porosity and has a high correlation. The original water saturation of the four types of pore structures was calculated to be 51.25, 56.13, 61.34, and 68.67%, respectively, based on different types of samples. The mercury pressure curve is processed by replacing the nonwetting phase saturation with the wetting phase saturation to obtain the pressure difference corresponding to different wetting phase saturations (water saturations).

The pressure difference corresponding to the original water saturation of 51.25% is 1.65 MPa (Fig. 13); that is, when the pressure difference is greater than 1.65 MPa, the gas production is accompanied by partial free water. The water saturation at which the water starts to flow is 26.9%, which corresponds to 5.3 MPa for the mercury pressure curve. When it is greater than 5.3 MPa, the water is converted from irreducible to movable. The gas production pressure difference corresponding to type I pores is 10.45 MPa, and the corresponding wetting phase saturation is 12.7%. That is, when the pressure difference is greater than 10.45 MPa, at most 87.3% of the nonwetting phase is involved in the flow, while 12.7% of the wetting phase fluid remains in the pores due to the capillary pressure.

Similarly, the mercury injection curves and relative permeability curves of type II, III, and IV pore structures were compared to obtain Fig. 13. Influenced by the pore structure, the movable fluid saturation of type III pores is small, with an original water saturation of 61.34%, an irreducible water saturation of 31.7%, a free water saturation of 29.64%, a movable water saturation of 18.84%, and an immovable fluid saturation of 10.8% in the free water. Combined with the relative permeability, when the pressure difference is between 0.58 MPa and 7.9 MPa, the produced water is a small amount of residual working fluid and condensate water. When the pressure difference is between 7.9 MPa and 13.3 MPa, the produced water type is the movable part of free water. With the decrease in pressure, the residual part of the free water is converted into movable water via seepage when the pressure difference is greater than 13.3 MPa.

The type IV pore space has the smallest movable fluid saturation (<20%), with a 68.67% original water saturation, 33.8% irreducible water saturation, and 34.87% free water saturation. Combined with the relative permeability, when the pressure difference is between 1.46 MPa and 11.7 MPa, the produced water is a small amount of residual working fluid and condensate water with residual gas. The well corresponding to such pores is characterized by a high residual gas saturation and low gas–water ratio or even pure water production at the later stage of production.
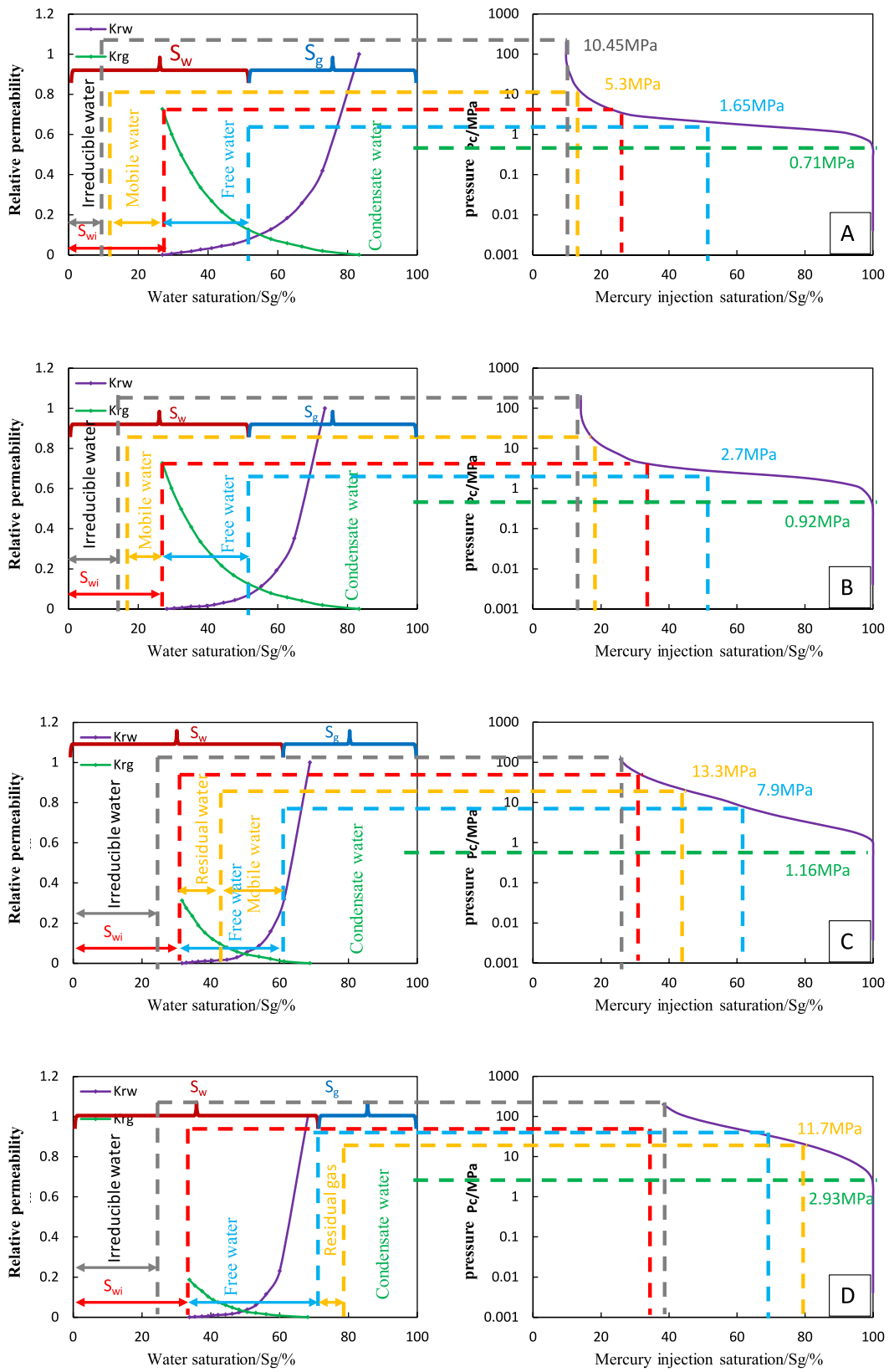
Fig. 13 Corresponding pictures of the relative permeability curve and mercury injection curve in various pores (**A** type I; **B** type II; **C** type III; **D** type IV)

The results of the gas–water seepage corresponding to different types of pore structures show that as the pore structure becomes worse, transiting from type I to IV, the fluid seepage resistance increases, the movable fluid saturation decreases, the residual water saturation gradually increases, and then the residual gas increases, corresponding to a pressure relief experiment in which the pressure remains high.

The above studies were combined to determine the nodal production pressure difference for the conversion of irreducible to moveable water of different types (Fig. 13). The field results show that as the properties of the reservoir worsen, the production pressure difference of wells increases, and the water production increases significantly. Therefore, the production pressure difference should be controlled appropriately during production to maximize productivity.

Conclusions

1. Quartz sandstone and lithic quartz sandstone are developed in the study area. The reservoir developed mainly intergranular dissolved pores and dotted and flaky pore throats, the pore throat size is small (mainly microthroats), and the pore throat structure can be divided into four categories.
2. The type I pores mainly have membrane residual water, the smallest fluid percolation resistance, the best flow capacity, and the largest range of the two-phase coseepage area. The transition of the gas–water displacement mode is shown as follows: uniform→reticular→fingering.
3. The water saturation of original, irreducible, movable, and free is 51.25%, 26.93%, 14.2%, and 24.35%. When the pressure difference is 0.35 ~ 1.65 MPa, the type of water produced is a small amount of residual working fluid and condensate water. As the formation pressure decreases, part of the irreducible water is converted into movable water.
4. The wells in a type IV pore structure have low productivity during water production and even shut down. A reasonable development pattern should be carried out, and the production pressure difference should be strictly controlled to maximize productivity.

Declarations

References

Al-Fatlawi O, Hossain M, Essa A (2019) Optimization of fracture parameters for hydraulic fractured horizontal well in a heterogeneous tight reservoir: an equivalent homogeneous modelling approach. SPE Kuwait Oil Gas Show Conf. https://doi.org/10.2118/198185-MS

Cai YD, Liu DM, Pan ZJ, Che Y, Liu ZH (2016) Investigating the effects of seepage-pores and fractures on coal permeability by fractal analysis. Transp Porous Media 111(2):479–497. https://doi.org/10.1007/s11242-015-0605-7

Clarkson CR, Solano N, Bustin RM, Bustin AMM, Chalmers GRL (2013) Pore structure characterization of North American shale gas reservoirs using USANS/SANS, gas adsorption, and mercury intrusion. Fuel 103:606–616. https://doi.org/10.1016/j.fuel.2012.06.119

Dai JX, Ni YY, Wu XQ (2012) Tight gas in China and its significance in exploration and exploitation. Pet Explor Dev 39(3):277–284. https://doi.org/10.1016/S1876-3804(12)60043-3

Dheyauldeen A, Al-Fatlawi O, Hossain MM (2021) Incremental and acceleration production estimation and their effect on optimization of well infill locations in tight gas reservoirs. J Pet Explor Prod Technol 11(6):2449–2480. https://doi.org/10.1007/s13202-021-01179-1

Dou HG, Yang Y (2012) Further understanding on fluid flow through multi-porous media in low-permeability reservoirs. Pet Explor Dev 39(5):674–682. https://doi.org/10.1016/S1876-3804(12)60092-5

Dou WC, Liu LF, Wu KJ, Xu ZJ (2018a) Diagenetic heterogeneity, pore throats characteristic and their effects on reservoir quality of the upper Triassic tight sandstones of Yanchang formation in Ordos Basin, China. Mar Pet Geol 98:243–257. https://doi.org/10.1016/j.marpetgeo.2018.08.019

Dou WC, Liu LF, Wu KJ, Xu ZJ, Feng X (2018b) Diagenesis of tight oil sand reservoirs: upper Triassic tight sandstones of Yanchang formation in Ordos Basin, China. Geol J 53(2):707–724. https://doi.org/10.1002/gj.2922

Gao YL, Li P, Li T (2021) Influence of different pore structure types on the occurrence features of movable fluid in Chang-10 reservoir in

Wuqi-Ansai Oilfield. J Pet Explor Prod 11(4):1609–1620. https://doi.org/10.1007/s13202-021-01128-y

Guo S, Lyu XX, Zhang Y (2018) Relationship between tight sandstone reservoir formation and hydrocarbon charging: a case study of a Jurassic reservoir in the eastern Kuqa depression, Tarim basin, NW China. J Nat Gas Sci Eng 52:304–316. https://doi.org/10.1016/j.jngse.2018.01.031

Guo XD, Lv M, Cui HJ, Lei KY (2023) A new method of evaluating well-controlled reserves of tight gas sandstone reservoirs. J Pet Explor Prod Technol 13(4):1085–1097. https://doi.org/10.1007/s13202-022-01584-0

He J, Liu XD, Zhu XY, Jiang T, He H (2021a) Experimental study on the two-phase seepage law of tight sandstone reservoirs in Ordos Basin. J Energy Eng-ASCE. https://doi.org/10.1061/(ASCE)EY.1943-7897.0000797

He J, Liu XD, Zhu XY, Jiang T, He H (2021b) Water-flooding characteristics of lithologic reservoir in Ordos Basin. Sci Rep 11(1):2503. https://doi.org/10.1038/s41598-021-82035-4

He J, Liu ZW, Zhang H, Xie SH (2023) Study on development methods of different types of gas wells in tight sandstone gas reservoirs. Sci Rep. https://doi.org/10.1038/s41598-023-43640-7

Li H, Yue D, Zhang X (2012) Characteristics of pore structure and reservoir evaluation of low permeability reservoir in Sulige gas field. Earth Sci Front 19(2):133–140

Li P, Zheng M, Bi H, Wu ST, Wang XR (2017) Pore throat structure and fractal characteristics of tight oil sandstone: a case study in the Ordos Basin. China J Pet Sci Eng 149:665–674. https://doi.org/10.1016/j.petrol.2016.11.015

Liang Y, Wang S, Feng Q, Zhang M (2023) Ultrahigh-resolution reconstruction of shale digital rocks from FIB-SEM images using deep learning. SPE J. https://doi.org/10.2118/218397-PA

Liu MJ, Xiong C (2021) Diagenesis and reservoir quality of deep-lacustrine sandy-debris-flow tight sandstones in Upper Triassic Yanchang formation, Ordos Basin, China: implications for reservoir heterogeneity and hydrocarbon accumulation. J Pet Sci Eng 202:108548. https://doi.org/10.1016/j.petrol.2021.108548

Liu D, Sun W, Ren D, Zhang X (2016) Features of pore-throat structures and movable fluid in tight gas reservoir: a case from the 8th member of Permian Xiashihezi formation and the 1th member of Permian Shanxi formation in the western area of Sulige Gasfield, Ordos Basin. Nat Gas Geosci 27(12):2136–2146

Liu MJ, Liu Z, Wu YW, Zhu WQ, Wang P (2017) Differences in formation process of tight sandstone gas reservoirs in different substructures in Changling fault depression, Songliao Basin, NE China. Pet Explor Dev 44(2):257–264. https://doi.org/10.1016/S1876-3804(17)30028-9

Liu XF, Kang YL, Li JF, Chen ZJ (2020) Percolation characteristics and fluid movability analysis in tight sandstone oil reservoirs. ACS Omega 5(24):14316–14323. https://doi.org/10.1021/acsomega.0c00569

Mohammadi S, Kharrat R, Khalili M, Mehranfar M (2011) Optimal conditions for immiscible recycle gas injection process: a simulation study for one of the Iranian oil reservoirs. Sci Iran 18(6):1407–1414. https://doi.org/10.1080/10916466.2011.557680

Rafieepour S, Zheng D, Miska S, Ozbayoglu E (2020) Combined experimental and well log evaluation of anisotropic mechanical properties of shales: an application to wellbore stability in bakken formation. SPE Ann Tech Conf Exhib. https://doi.org/10.2118/201334-MS

Shabani B, Kazemzadeh E, Entezari A, Aladaghloo J, Mohammadi S (2014) The calculation of oil-water relative permeability from capillary pressure data in an oil-wet porous media: case study in a dolomite reservoir. Pet Sci Technol 32(1):38–50

Shang T, Cao H, Guo Y, Wu H (2017) Microscopic pore structure characteristics and its effects on reservoir quality: a case study from Shanxi formation of upper Paleozoic in Yanchang exploration area in Ordos Basin. J Northwest Univ Nat Sci Edn 47(6):877–886

Su HB, Dong YJ, Song FQ (2014) Numerical simulation of the nonlinear flow in tight sandstone reservoirs. In: 4th international symposium on multi-field coupling theory of rock and soil media and its applications. St Plum-Blossom Press Pty Ltd, Zhoushan City, PEOPLES R CHINA, pp. 132–139

Wang H, Ji BY, Lv CY, Zhang L (2019) The stress sensitivity of permeability in tight oil reservoirs. Energy Explor Exploit 37(4):1364–1376. https://doi.org/10.1177/0144598719855819

Wang S, Liang YP, Feng QH, Javadpour F (2022) Sticky layers affect oil transport through the nanopores of realistic shale kerogen. Fuel. https://doi.org/10.1016/j.fuel.2021.122480

Wu HY, Dong XS, Xu Y, Xiong G (2021) Seepage mechanism of tight sandstone reservoir based on digital core simulation method. Appl Sci 11(9):3741. https://doi.org/10.3390/app11093741

Zhang SH, Tang SH, Zhang JP, Pan ZJ (2018) Pore structure characteristics of China sapropelic coal and their development influence factors. J Nat Gas Sci Eng 53:370–384

Zhao YL, Zhang LY, Wang YX, Lin H (2023) Thermal-hydraulic-mechanical (THM) coupling behaviour of fractured rock masses. Geofluids. https://doi.org/10.1155/2023/9764934

Zheng D, Miska S, Ziaja M, Zhang J (2019) Study of anisotropic strength properties of shale. AGH Drill Oil Gas. https://doi.org/10.56952/ARMA-2023-0128

Zheng D, Miska S, Ozbayoglu E, Zhang J (2023a) Combined experimental and well log study of anisotropic strength of shale. SPE Ann Tech Conf Exhib. https://doi.org/10.2118/214981-MS

Zheng D, Ozbayoglu E, Miska S, Zhang J (2023b) Experimental study of anisotropic strength properties of shale. The University of Tulsa

Zhou Y, Zhang GZ, Liu JZ (2022) Modeling method to characterize the pore structure of fractured tight reservoirs. Appl Sci 12(4):2078. https://doi.org/10.3390/app12042078

Zou CN, Zhu RK, Liu KY, Su L (2012) Tight gas sandstone reservoirs in China: characteristics and recognition criteria. J Pet Sci Eng 88–89:82–91. https://doi.org/10.1016/j.petrol.2012.02.001